Article

Not peer-reviewed version

MOF-Derived Spindle-Shaped Z-Scheme ZnO/ZnFe2O4 Heterojunction: A Magnetic Recovery Photocatalyst for Efficient Tetracycline Hydrochloride Degradation

Shilong Suo , Wenmei Ma , Pengfei Fang * , Siyi Zhang , Ziwu Han , Yumin Wang , Yuanyuan Li , Yi Xiong , Yong Liu , Chunqing He

Posted Date: 22 September 2023

doi: 10.20944/preprints202309.1580.v1

Keywords: Z-scheme; Tetracycline; Photocatalysis; ZnFe2O4; ZnO

Article

MOF-Derived Spindle-Shaped Z-Scheme ZnO/$ZnFe_2O_4$ Heterojunction: A Magnetic Recovery Photocatalyst for Efficient Tetracycline Hydrochloride Degradation

Shilong Suo [1], Wenmei Ma [1], Siyi Zhang [1], Ziwu Han [1], Yumin Wang [1], Yuanyuan Li [1], Yi Xiong [2], Yong Liu [1], Chunqing He [1] and Pengfei Fang [1,*]

[1] School of Physics and Technology, Key Laboratory of Nuclear Solid State Physics Hubei Province, Wuhan University, Wuhan 430072, China; fangpf@whu.edu.cn (P.F.)
[2] School of Mathematical & Physical Sciences, Department of Microelectronics, Wuhan Textile University, Wuhan 430073, China; xiong@wtu.edu.cn (Y.X.)
* Correspondence: fangpf@whu.edu.cn

Abstract: The development of photocatalysts with a wide spectral response and effective carrier separation capability is essential for the green degradation of tetracycline. In this work, a magnetic recyclable Z-scheme ZnO/$ZnFe_2O_4$ heterojunction (ZZF) was successfully constructed by the solid phase method using MIL-88A(Fe)@Zn as the precursor. Appropriate band gap width and Z-scheme charge transfer mechanism make ZZF have excellent visible light absorption performance, efficient charge separation and strong redox ability. Under visible light irradiation, the degradation efficiency of TCH for optimal sample ZZF2 can reach 86.3% within 75 min in deionized water, and achieve 92.9% within 60 min in tap water, which exhibits superior stability and reusability after five cycles. Moreover, the catalyst in the water can be conveniently recovered by magnetic force. After visible light irradiation for 70 minutes, the temperature of the reaction system increased by 21.9 °C. Its degradation constant (35.53×10^{-3} min^{-1}) increases 5.1 times that at room temperature (6.95×10^{-3} min^{-1}). Thermal energy perfects the kinetic driving force of the reactants and promotes carrier migration to produce more $\bullet O_2^-$ and •OH. This work provides a potential candidate and inspires the design of photocatalyst for tetracycline hydrochloride degradation.

Keywords: Z-scheme; Tetracycline; Photocatalysis; $ZnFe_2O_4$; ZnO

1. Introduction

Antibiotics are widely used for promoting plant growth and controlling disease outbreaks. Tetracycline hydrochloride (TCH), as a broad-spectrum antibiotic, is used in disease treatment and the aquaculture industry [1]. However, it cannot be fully metabolized in living organisms, and the residual amount of TCH in the environment is increasing [2]. Recent years, TCH and its metabolites have been detected in surface water, groundwater, and drinking water [3–5]. At present, antibiotics represented by TCH have been one of the most important pollutants in water [6]. Therefore, it is necessary to establish a feasible solution to degrade TCH in water.

Photocatalysis technology is currently the most promising approach to degrade TCH in water because it is environmentally friendly and low-cost [7,8]. However, photocatalysis technology requires the absorption of photons with energies greater than the semiconductor band gap to produce electron-hole pairs, which then migrate to the surface to form active substances [9], such as $\bullet O_2^-$, •OH, etc. This leads to two bottlenecks in the photocatalysis technology, one is the low utilization of sunlight [10] (no more than 5%), and the other is the easy recombination of carriers [11–13], resulting in low photocatalytic efficiency. To solve the above problems, a variety of strategies including element doping and heterojunction construction have been developed [14–22]. Among them, the

 doi:10.20944/preprints202309.1580.v1

construction of heterojunction is a research hotspot [23]. In recent years, the visible light degradation of TCH by constructing different heterojunction photocatalysts has been extensively studied [16]. For example, Guo et al. [24] prepared a 2D/2D Z-scheme $CuInS_2$/g-C_3N_4 photocatalyst, which achieved 83.7% degradation efficiency of TCH under visible. Li et al. [10] reported a BP/BiOBr S-scheme heterojunction to improve photocatalytic activity and achieved 85% degradation efficiency of TCH under visible light.

Although the heterojunction can accelerate the carrier separation efficiency, the upper utilization of sunlight is limited by the band gap width [13]. In 2015, Hu raised the main contradiction of photocatalysts: the absorption of photons requires a small band gap, while sufficient potential energy to drive the photocatalytic reaction needs a large band gap [25]. This is an "intrinsic" contradiction that cannot be resolved through energy band engineering [13]. To compensate for this, Hu et al. compensate for the lack of reaction potential energy by introducing thermal energy [25]. Thermal energy can be derived from infrared light and electron-hole pair recombination that without requiring additional input energy. Up to now, photothermal catalysis has been widely used in CO_2 reduction [26,27], hydrogen evolution [28,29], pollutant degradation [30,31], organic synthesis [32,33], and many other aspects because of its advantages in promoting carrier separation and migration [26,34,35], enhancing kinetic driving force [13,36] and adjusting redox potential of half reactions [27,37]. Fang et al. [38] reported the photothermal catalyst WS_2, achieved 87.4% degradation efficiency of TCH under visible light, which was 2.4 times and 3.5 times higher than that of thermal catalysis alone and room temperature photocatalysis, respectively, achieving a catalytic effect of overall greater than the partial sum.

$ZnFe_2O_4$ is a common magnetic semiconductor with a narrow band gap (≈1.9 eV), low price, and excellent photochemical stability [39–41]. The magnetic properties make it easy and economical to recover from the liquid phase [42]. At the same time, magnetism can also change the spin polarization of electrons and promote the separation of electron-hole pairs. [39]. The Fe element in $ZnFe_2O_4$ has the potential for the Fenton reaction [41,43]. These advantages make it receive more and more attention [44–47]. For example, Fei et al. [48]. synthesized $ZnFe_2O_4$/In_2O_3 Z-scheme heterojunctions. Their excellent carrier separation efficiency made them exhibit excellent photocatalytic activity and stability during TCH degradation. Yang et al. [49] used the intrinsic catalytic behavior of $ZnFe_2O_4$ similar to peroxidase to efficiently and persistently hydroxyl benzene into phenol.

To sum up, we cleverly designed and synthesized a magnetic recyclable ZnO/$ZnFe_2O_4$ heterojunction photocatalysts with Z-scheme charge transfer mechanism and excellent photothermal conversion capability. The morphology, structure and chemical state of the elements of the as-prepared photocatalyst were studied by scanning electron microscope (SEM), high-resolution transmission electron microscope (HRTEM), X-ray diffraction (XRD) patterns and X-ray photoelectron spectroscopy (XPS) tests. Subsequently, we systematically evaluated the photocatalytic activity and stability of as-prepared photocatalysts using TCH as a probe. As expected, the ZZF photocatalyst showed excellent photocatalytic performance and stability. The band structure was studied by Mott-Schottky (M-S) plots and UV-visible diffuse reflectance (DRS) spectra. The main active species were ascertained by the terephthalic acid photoluminescence (TA-PL) experiment, electron spin resonance (ESR) test, and free radical capture experiment. Combined with the band structure and the active substances produced during the reaction, the carrier transfer pathways were determined as the Z-scheme mechanism. This work aims to provide ideas for designing photocatalysts with excellent antibiotic degradation performance.

2. Materials and Methods

2.1. Materials

All of the following reagents were offered by Sinopharm Chemical Reagent Co., Ltd. and used as received without further purification: ferric chloride hexahydrate ($FeCl_3$•$6H_2O$), fumaric acid ($C_4H_4O_4$), dimethyl formamide (DMF), silver nitrate ($AgNO_3$), isopropyl alcohol (IPA), zinc nitrate hexahydrate ($Zn(NO_3)_2$•$6H_2O$), terephthalic acid (TA), triethanolamine (TEOA), sodium chloride

Preprints (www.preprints.org) | NOT PEER-REVIEWED | Posted: 22 September 2023 doi:10.20944/preprints202309.1580.v1

(NaCl), potassium chloride (KCl), sodium sulfide (Na_2S), sodium sulfate (Na_2SO_4), sodium hypochlorite (NaClO), potassium permanganate ($KMnO_4$) sodium nitrate ($NaNO_3$), hydrochloric acid (HCl), sodium hydroxide (NaOH). Tetracycline hydrochloride (TCH) was purchased from Aladdin Industrial Corporation. P-benzoquinone (BQ) was purchased from Shanghai Macklin Biochemical Co., Ltd. The deionized water (DI water, 18.3 MΩ•cm resistivity) was produced from the deionizer (PGDX-S-10B, Pinguanwater Co, Ltd., China). Tap water and lake water from Wuhan, Hubei, China.

2.2. Preparation of MIL-88A(Fe)

MIL-88A(Fe) were synthesized according to a modified method of the literature reported [50]. Firstly, 2.7050 g $FeCl_3$•$6H_2O$ and 1.16072 g $C_4H_4O_4$ were dissolved in 50 mL DMF. Subsequently, the mixed solution heated at 100 °C for 12 h in a 100 mL reactor, and then the precipitate was washed with DMF and ethanol several times. Eventually, the resulting product was soaked in DI water for 12 h to remove DMF, and then dried at 120 °C for 12 h.

2.3. Preparation of ZnO/$ZnFe_2O_4$

MIL-88A(Fe) and 0.5950 g $Zn(NO_3)_2$•$6H_2O$ was mixed in 15 mL DI water and then all the water was dried to prepare MIL-88A(Fe)@Zn. Subsequently, MIL-88A(Fe)@Zn was heated in quartz tube furnace to 600 °C at a heating rate of 5 °C/min and maintained for 6 h, ZnO/$ZnFe_2O_4$ was obtained after natural cooling. The masses of the added MIL-88A(Fe) was 1.6560 g, 0.8280 g, and 0.4140 g, and is recorded as ZZF1, ZZF2, and ZFF3, respectively. For comparison, ZnO was obtained without adding MIL-88A. $ZnFe_2O_4$ (ZFO) was prepared by adding 1.9044 g MIL-88A.

2.4. Photocatalyst Characterizations, Photocatalytic (Photoelectrochemical) Test, and Photothermal Conversion Performance

The photocatalyst characterizations, photocatalytic (photoelectrochemical) test, and photothermal conversion performance are fully detailed in the Supplementary Material.

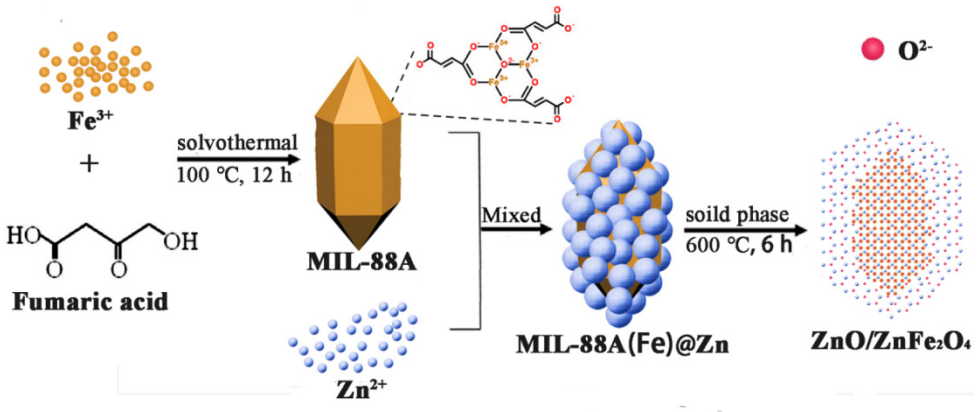

Figure 1. Schematic illustration for the preparation process of ZnO/$ZnFe_2O_4$ heterojunction.

3. Results and Discussion

3.1. Morphology and Structure

To investigate the morphology and structure of ZnO/$ZnFe_2O_4$ heterojunction, ZZF2 and its precursors were analyzed by SEM and HRTEM. As shown in Figure 2a, MIL-88A (Fe) has a spindle-shaped structure with a length and width of about 500 nm and 300 nm. After MIL-88A(Fe) is mixed with zinc nitrate, zinc nitrate is uniformly attached to the surface of MIL-88A(Fe) to form MIL-88A(Fe)@Zn (Figure 2b). As can be seen from Figure 2c, the surface of the ZZF2 becomes rough after annealing, and the spindle structure is slightly damaged. From Figure 2d, the ZZF2 sample has

 doi:10.20944/preprints202309.1580.v1

obvious lattice fringes with crystal fringe spacing of 0.292 nm, 0.489 nm, and 0.284 nm, which corresponds perfectly to the (220), (111) crystal faces of $ZnFe_2O_4$ and the (100) crystal faces of ZnO, respectively. The EDX spectra (Figure S1a) and EDX mapping (Figure 2e) of the ZZF2 composite verified the presence of only Zn, Fe, and O elements. The thermogravimetric curve of MIL-88A (Fe)@Zn (Figure S1c) shows that the weight of the precursor steadily decreases with increasing temperature. This means that the adsorbed water, C and N elements in the precursor are progressively released. The mass does not change after the temperature reaches 500 °C, indicating that the precursor has become a stable inorganic substance. The EDX mapping shows that the distribution of Zn and Fe elements in the ZZF2 is not synchronous, indicating that ZnO/$ZnFe_2O_4$ heterostructures have been successfully constructed.

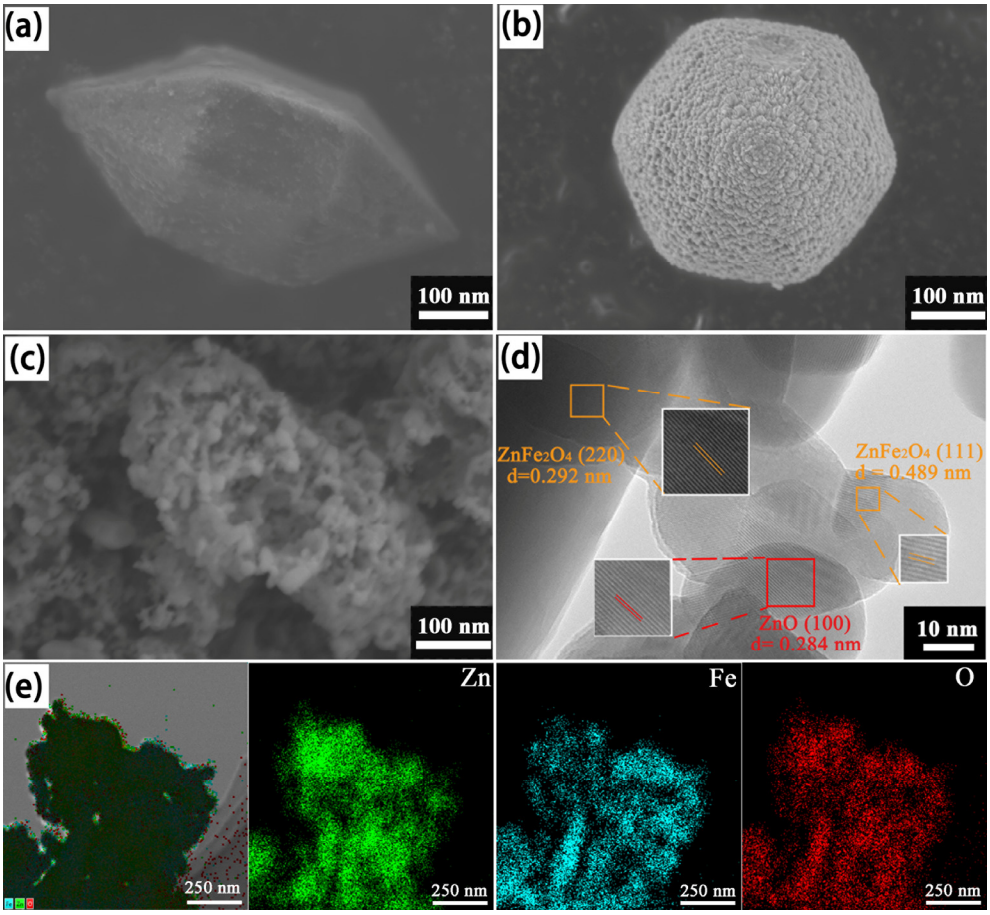

Figure 2. SEM images of (**a**) MIL-88A(Fe), (**b**) MIL-88A(Fe)@Zn, and (**c**) ZZF2; HRTEM images of (**d**) ZZF2; (**e**) EDX mapping result of Zn, Fe, and O of the ZZF2.

As shown in Figure 3, the crystal phase and crystallinity of as-prepared are determined XRD patterns. The peaks of hexagonal wurtize ZnO at 2θ values of 31.76°, 34.42°, 36.25°, 47.54°, 56.5°, 62.85°, 67.94° and 69.08° referred to the *hkl* indices (100), (002), (101), (102), (110), (103), (112) and (201), respectively (PDF#99-0111). Similarly, the peaks of cubic spinel crystal $ZnFe_2O_4$ was observed of 2θ at 29.82°, 35.21°, 42.69°, 53.32°, 56.52° and 62.12° which is the index to (220), (311), (400), (422), (511) and (440) planes, respectively (PDF#22-1012). The diffraction peaks of ZnO and ZFO appear simultaneously in samples ZZF1, ZZF2, and ZZF3, and the peaks do not shift. It shows that the crystal lattice of the semiconductor is not destroyed when the heterojunction is formed. This is advantageous for photogenerated carrier migration. With the increase of Zn element, the peak strength representing ZnO gradually increases and the peak position representing ZFO gradually decreases in XRD spectra. All peaks are sharp, indicating that the synthesized sample has excellent crystallinity.

Preprints (www.preprints.org) | NOT PEER-REVIEWED | Posted: 22 September 2023 doi:10.20944/preprints202309.1580.v1

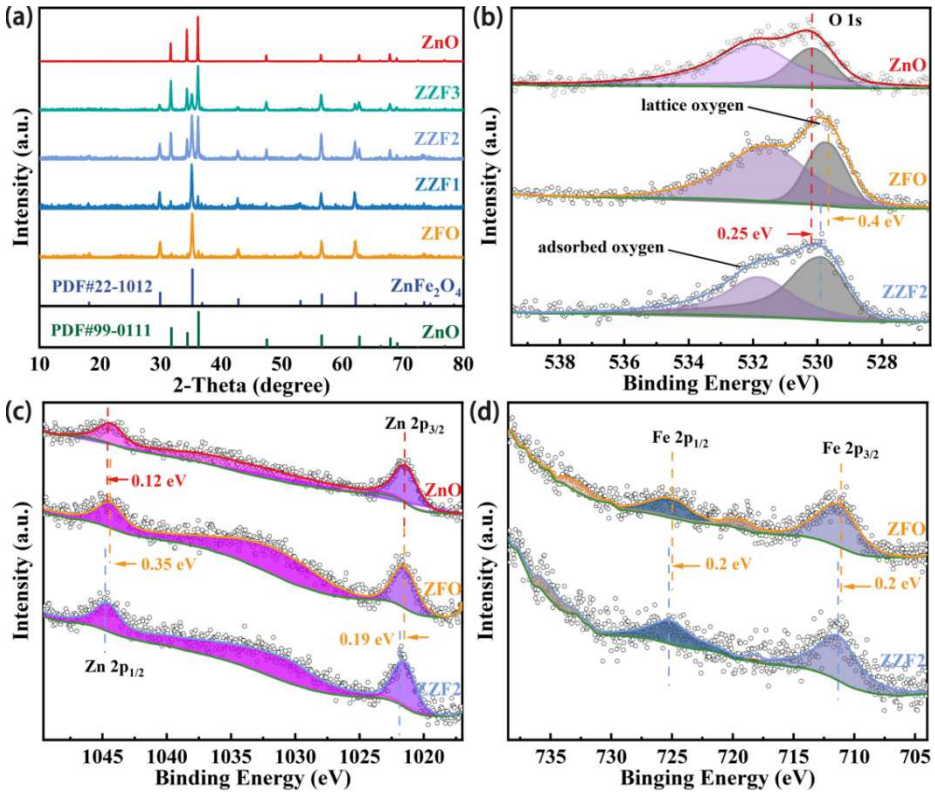

Figure 3. (**a**) XRD patterns of ZnO, ZZF samples, and $ZnFe_2O_4$. XPS spectra related to (**b**) O 1s, (**c**) Zn 2p, (**d**) Fe 2p of $ZnFe_2O_4$, ZZF2, and ZnO samples, respectively.

The surface element composition and chemical state of the ZnO, ZZF2 and ZFO were further characterized by XPS. All binding energy (BE) values were calibrated by C 1s peak at 284.8 eV. As shown in Figure S2, the existence of Zn, Fe, and O elements in ZZF2. Two convolution peaks can be fitted in the O 1s spectra in Figure 3b. These two peaks represent surface adsorbed oxygen (at about 531.5 eV) and lattice oxygen (at about 529.7 eV), respectively [39,40]. In the high-resolution spectra of Zn 2p, the BE of Zn $2p_{3/2}$ changes from 1021.63 eV (ZnO) and 1021.46 eV (ZFO) to 1021.65 eV (ZZF2), respectively. Similarly, the BE of Zn $2p_{1/2}$ shifts from 1044.59 eV (ZnO) and 1044.36 eV (ZFO) to 1044.71 eV (ZZF2), respectively. The higher BE of ZZF2 indicates that the Zn element loses electrons during the formation of heterojunctions. The BE of Fe $2p_{3/2}$ and Fe $2p_{1/2}$ in ZFO are 711.11 eV and 724.91 eV, respectively, corresponding to the characteristic peak of Fe^{3+}. After forming the ZZF2 sample, the BE shifts to 711.51 eV and 725.11 eV, respectively. The BE of Zn and Fe elements in the ZZF2 sample are slightly higher than ZnO and ZFO. The change of chemical state further verifies the successful synthesis of heterojunction [18,39].

3.2. Photocatalytic Activity and Reusability

Through the experimental study of photocatalytic degradation of TCH under visible light irradiation, the activity of the as-prepared photocatalysts was evaluated (Figure 4a). Obviously, the degradation efficiency of all ZZF samples for TCH is higher than that of pure ZnO and ZFO, indicating that the construction of heterojunction promotes the degradation of TCH. The ZZF2 samples showed the best photocatalytic activity after 75 minutes of visible light irradiation, and the degradation rate reached 86.3%. Further, it can be found that with the increase of the amount of $Zn(NO_3)_2 \bullet 6H_2O$, the photocatalytic efficiency increases first and then decreases. This is because with the increase of the amount of $Zn(NO_3)_2 \bullet 6H_2O$, the proportion of ZnO in the heterojunction gradually increases, and the band gap of ZnO is much wider than that of ZFO, which cannot effectively absorb photons, resulting in a decrease in the number of photogenerated charge carriers. Figure 4b shows

Preprints (www.preprints.org) | NOT PEER-REVIEWED | Posted: 22 September 2023 doi:10.20944/preprints202309.1580.v1

the reaction kinetics (k_{TCH}) of as-prepared photocatalysts, and the experimental data conform to the pseudo-first-order kinetics [39,47]:

$$\ln(C_0 / C) = kt \quad (1)$$

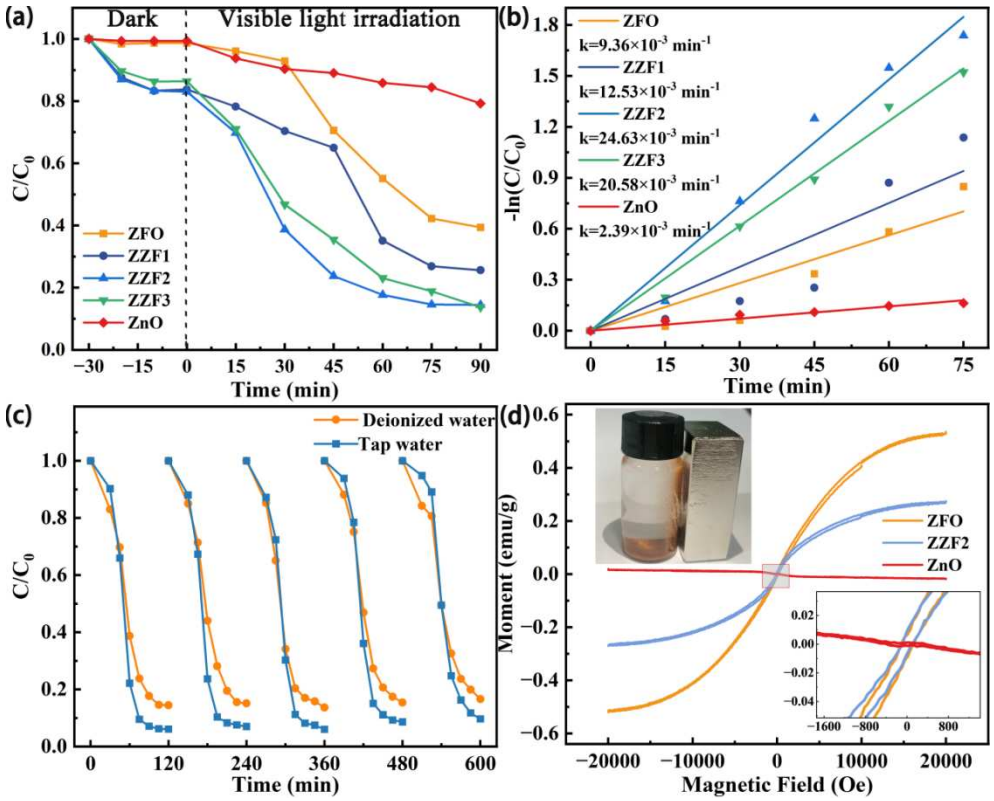

Figure 4. (**a**) Photocatalytic performance of TCH degradation, and (**b**) corresponding pseudo-first-order kinetics curves of as-prepared samples. (**c**) Cycling experiments of photocatalytic TCH degradation of ZZF2 in DI water and tap water. (**d**) Magnetic hysteresis loops of ZnO, $ZnFe_2O_4$, and ZZF2.

The k_{TCH} of ZFO, ZZF1, ZZF2, ZZF3 and ZnO are 9.36 × 10^{-3} min^{-1}, 12.56 × 10^{-3} min^{-1}, 24.63 × 10^{-3} min^{-1}, 20.58 × 10^{-3} min^{-1}, 2.39 × 10^{-3} min^{-1}, respectively. The k_{TCH} of ZZF2 is 2.63 times that of ZFO and 10.3 times that of ZnO. Compared with other photocatalysts, the degradation effect is still at a leading level (Table S1).

After evaluating the photocatalytic activity, the cyclic stability of ZZF2 in DI water and tap water were studied (Figure 4c). This is necessary for practical applications. After five cycles, the photocatalytic activity of the ZZF2 on TCH in DI water attenuated to 80% and maintained 92.6% of the maximal activity. In tap water, the degradation efficiency reached 92.9% in 60 mins, which was better than that of DI water. The efficiency remained at 83.74% after 5 cycles. The properties decay slightly faster than in DI water, leaving only 90.1% of the original. XRD results demonstrate that the crystal structure of the ZZF2 sample has no obvious change after the reaction (Figure S3). In conclusion, the ZZF2 has good photocatalytic activity and cycle stability.

We found that the degradation effect of the ZZF2 on TCH in tap water was better than that in DI water. The difference between tap water and DI water is the ion content and pH. The main ions contained in tap water are listed in Table S2. To determine the effect of ions in tap water on the degradation effect, we added different compounds to DI water for comparative experiments (Figure S4a,b). The results showed that most ions had no significant effect on catalytic performance. Even in the lake water also showed excellent degradation performance (Figure S4c). The ZZF2 was soaked in tap water for 2 h and then degraded TCH in DI water, and the performance was not enhanced (Figure S4c). Tap water did not affect the catalyst. The weak pH change may be the reason for the different

Preprints (www.preprints.org) | NOT PEER-REVIEWED | Posted: 22 September 2023 doi:10.20944/preprints202309.1580.v1

degradation performance. Figure S4d shows that The effect of pH on the degradation of the ZZF2 is very significant. In the alkaline environment, TCH exists in the monoanionic form, while in the neutral environment, TCH exists in the neutral form, pH = 7.7 is the critical point [41]. Tap water has a pH of 7.8, therefore, a small pH difference leads to a large increase in degradation.

As shown in Figure 4d, ZnO is diamagnetism, while ZFO and ZZF2 exhibit weak ferromagnetism. The coercivity of ZFO and ZZF2 is 108 Oe, and the saturation magnetization of ZFO and ZZF2 is 0.53 emu/g and 0.27 emu/g, respectively. For powdered photocatalysts, it is also important to cost-effectively separate them from water [51]. The ZZF2 samples are attracted to magnets in DI water, which means that the ZZF2 samples dispersed in water can be easy recovered by electromagnets. The secondary pollution of water body is avoided, and the reusability and economic benefit are improved.

3.3. Effect of Temperature on Catalytic Effect

As the reaction progresses, the temperature of the system gradually increases. To determine the effect of temperature on the catalytic performance of the ZZF2, the catalytic activity of the reaction system was studied by controlling the temperature at 5 °C, 15 °C, 25 °C, 35 °C, and 45 °C. The results showed that the degradation effect of the ZZF2 on TCH was gradually improved with the increase of temperature (Figure 5a,b).

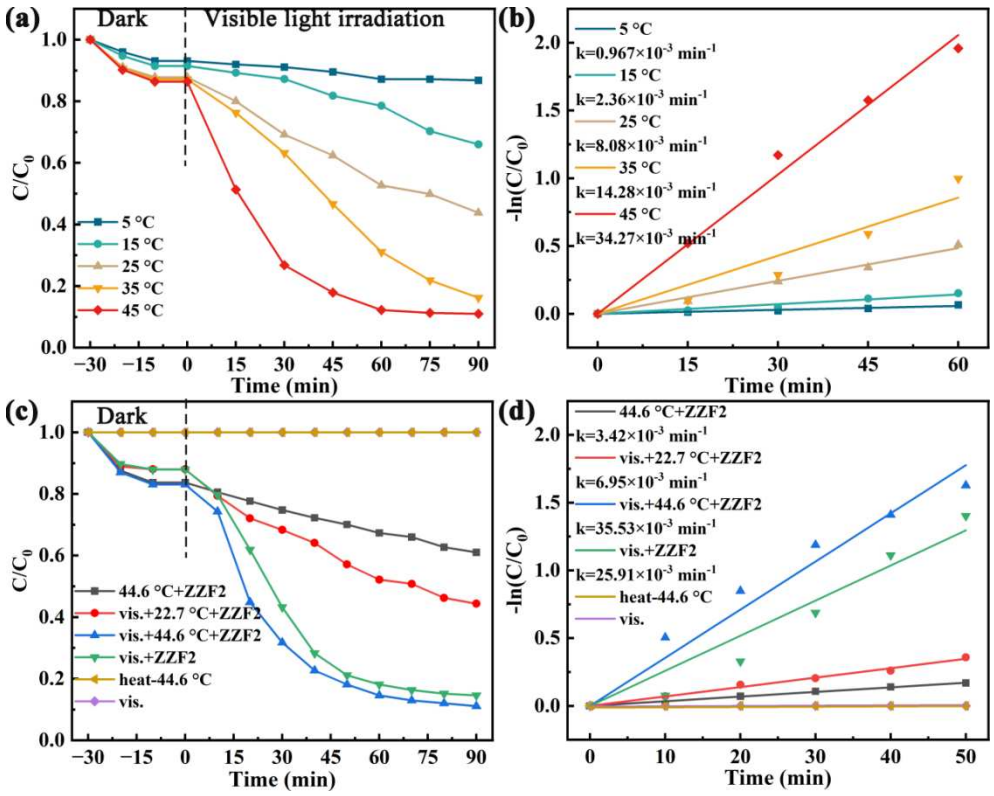

Figure 5. (**a**) Photodegradation performance of TCH degradation and (**b**) corresponding degradation rate constants of ZZF2 at different temperatures. (**c**) Photodegradation performance of TCH degradation and (**d**) corresponding degradation rate constants of ZZF2 at different conditions.

To explore the role of temperature, visible light, and catalyst in the reaction, we measured the TCH degradation rate under different conditions, and the results were show in Figure 5c**.** In the absence of catalyst, visible light irradiation and heating can not degrade TCH. Since the temperature of the reaction system under visible light irradiation can reach 44.6 °C, according to the principle of control variables, the temperature of photothermal catalysis and thermal catalysis is set at 44.6 °C. The degradation rate of TCH by the ZZF2 under thermo-assisted photocatalysis was significantly

Preprints (www.preprints.org) | NOT PEER-REVIEWED | Posted: 22 September 2023 doi:10.20944/preprints202309.1580.v1

higher than that under room-temperature photocatalysis and thermocatalysis. It can be seen from Figure 5d that the k_{TCH} of photothermal catalysis is 35.53×10^{-3} min^{-1}, while those of thermal catalysis and room-temperature photocatalysis are 3.42×10^{-3} min^{-1} and 6.59×10^{-3} min^{-1}, respectively. The catalytic effect that the whole is greater than the sum of parts is achieved [38]. Thermal energy not only degrades TCH but also promotes the photocatalytic reaction. If the temperature is not controlled, k_{TCH} gradually changed from 6.95×10^{-3} min^{-1} at 22.7 °C to 35.53×10^{-3} min^{-1} at 44.6 °C as the temperature rises during the reaction. The catalytic efficiency is increased by 5.1 times.

The photothermal conversion efficiency (η) and heating performance of the ZZF2 sample were further studied. The calculation method is detailed in Text S4. As shown in Figure S5, when the whole system reaches thermal equilibrium, the system temperature of adding the ZZF2 sample can reach 44.6 °C (η = 91.8%), pure DI water can only reach 33.1 °C (η = 27.9%). After adding the ZZF2 sample, the photothermal conversion efficiency was increased by 3.24 times. This shows that the ZZF2 sample can effectively convert the energy in simulated sunlight into thermal and chemical energy.

3.4. Analysis of the Photocatalytic Mechanism

To further understand the photocatalytic mechanism, we conducted free radical trapping experiments on the ZZF2 sample to determine the main active species in the photocatalytic degradation of TCH. The result is shown in Figure 6a. The isopropanol (IPA), P-benzoquinone (BQ), triethanolamine (TEOA), and silver nitrate ($AgNO_3$) was selected as the scavengers for •OH, $•O_2^-$, h^+ and e^-, respectively. Their corresponding amount is summarized in Table S3. After adding $AgNO_3$ and BQ, the degradation efficiency of TCH was greatly inhibited, indicating that e^- and $•O_2^-$ were the main active substances in the photocatalytic degradation of TCH in the ZZF2 sample. The addition of TEOA also affected the degradation rate, indicating that h^+ also played a role in the degradation process of TCH. However, the addition of IPA had little effect on the TCH degradation rate. To investigate whether •OH is produced during the reaction, the evolution of •OH fluorescence intensity with time was investigated by the TA-PL analysis method (Figure S6a**)**. As time goes on, the fluorescence intensity of •OH increased gradually. This indicates that •OH is produced during the reaction. Subsequently, to determine the effect of reaction conditions on the concentration of free radicals, we studied the fluorescence intensity of hydroxyl radicals under different conditions (Figure S6b). The results show that •OH is hardly produced by thermal catalysis. Under visible light irradiation, the concentration of •OH gradually increases with the increase of temperature. This shows that the promotion effect of temperature on photocatalysis is reflected in the production of more surface active substances on the catalyst surface. This can be attributed to heat-facilitated carrier separation and migration [13].

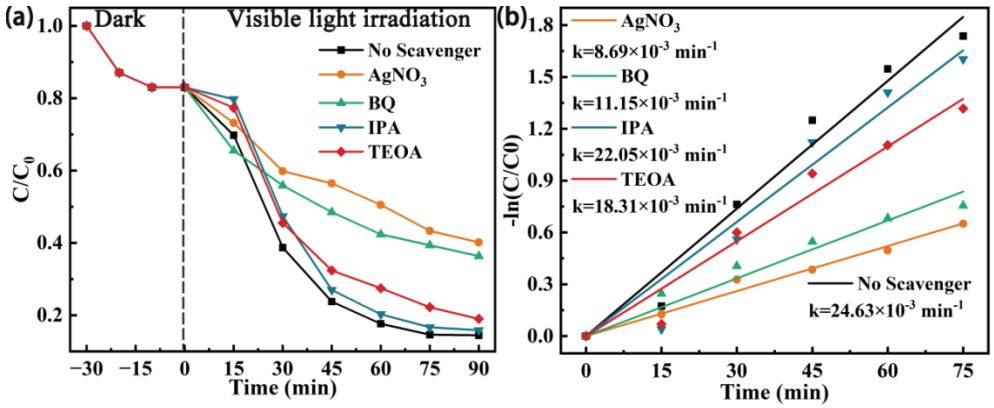

Figure 6. (**a**) The free radical trapping experiments for degradation of TCH over the ZZF2 sample and (**b**) corresponding pseudo-first-order kinetics.

For thermo-assisted photocatalysis degradation of TCH, the basic steps of catalysis are the same as those of traditional photocatalysis [13,40,52]. The band structure and charge separation capability

Preprints (www.preprints.org) | NOT PEER-REVIEWED | Posted: 22 September 2023 doi:10.20944/preprints202309.1580.v1

of catalysts were characterized by DRS, photoluminescence (PL) spectroscopy, and photoelectrochemical measurements. Figure 7a shows the DRS of a series of samples. Compared with pure ZnO, the absorption band edge of the catalyst supported with $ZnFe_2O_4$ has an obvious redshift. This means that the composite material has a greater ability to capture visible light. The absorption band edge of ZFO, ZZF1, ZZF2 and ZZF3 has no obvious change. The Tauc plots (Figure 7b) are obtained by converting the DRS data through the Kubelka-Munk formula:

$$\alpha h\nu^{1/n} = A(h\nu - E_g) \quad (2)$$

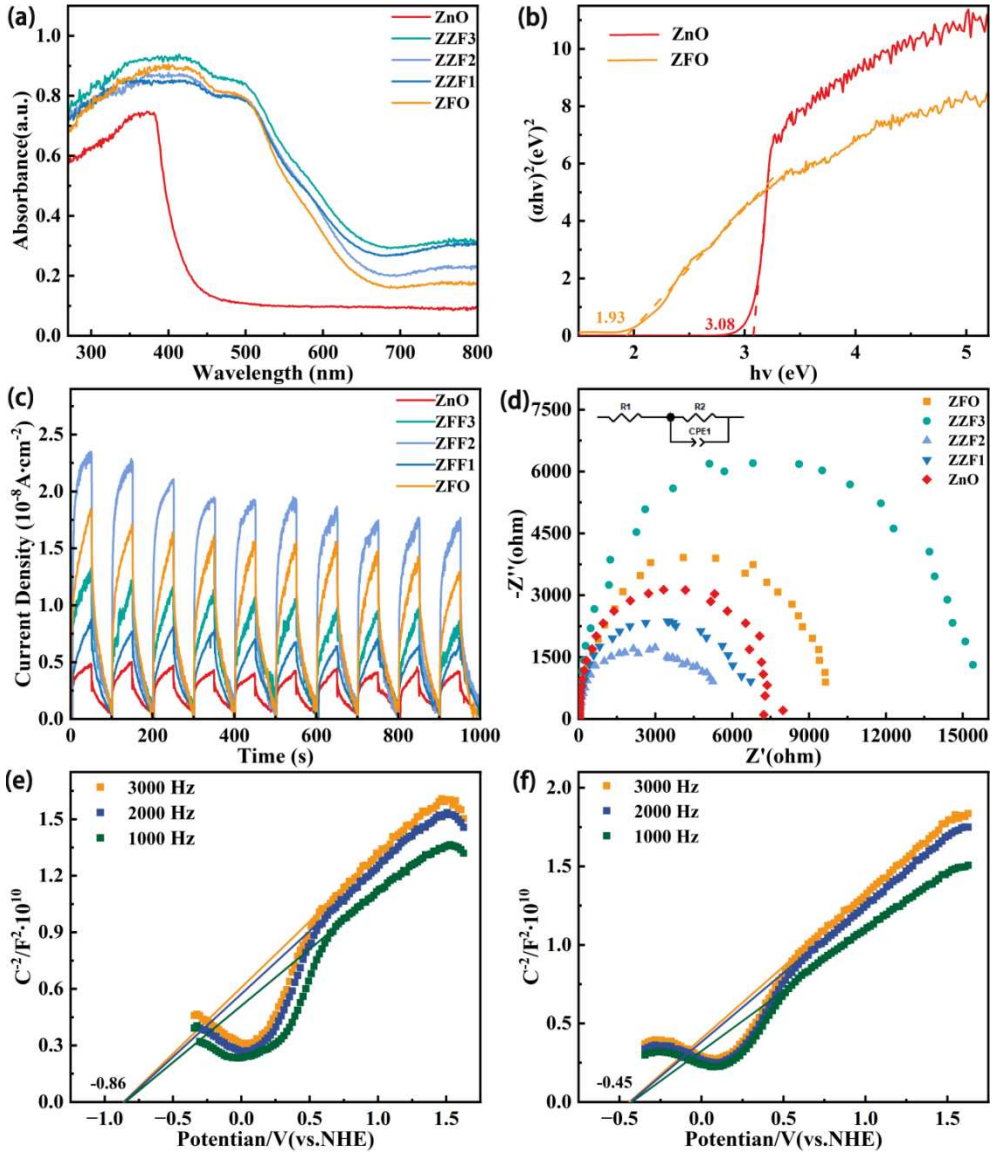

Figure 7. (**a**) The DRS spectra of ZnO, ZFF samples and $ZnFe_2O_4$. (**b**) Tauc plots of ZnO and $ZnFe_2O_4$. (**c**) Transient photocurrent density responses and (**d**) EIS Nyquist plots irradiated conditions of ZnO, ZFF samples and $ZnFe_2O_4$. M-S plots of (**e**) $ZnFe_2O_4$ and (f) ZnO.

For direct bandgap semiconductors, n=1/2. The bandgap energy (E_g) values of ZnO and ZFO are 3.08 eV and 1.93 eV, respectively. Which is consistent with previous reports [40]. PL spectra (Figure S7) show that ZnO has strong excitation light, but for ZZF2, the excitation light is very small. It is further proved that the heterojunction construction can effectively enhance the photogenerated carrier migration dynamics.

Figure 7c shows transient photocurrent density responses of a series of samples. The results show that the transient photocurrent of ZFF2 sample is significantly higher than that of ZnO and ZFO

Preprints (www.preprints.org) | NOT PEER-REVIEWED | Posted: 22 September 2023 doi:10.20944/preprints202309.1580.v1

sample. Heterojunction formation enhances photogenerated carrier dynamics. The transient photocurrent of ZFO is higher than ZZF1 and ZZF3 samples, but the catalytic efficiency is lower than ZZF1 and ZZF3 samples. It shows that the band structure of pure ZFO samples is not suitable, and the photogenerated carrier's redox ability is weak. Figure 7d and Figure S8 show the electrochemical impedance spectra under visible light irradiation and darkness, respectively. The ZZF2 sample has the smallest arc radius of all the samples. The arc radius of the series of samples is lower under visible light irradiation than in the dark. A smaller arc radius means a smaller charge transfer resistance [50]. Figure 7e,f is Mott-Schottky plots of ZFO and ZnO, respectively. The slope is positive which means they are all n-type semiconductors. And flat-band potential of ZFO and ZnO are located at -0.86 V vs. NHE and -0.45 V vs. NHE, respectively. For n-type semiconductors, their conduction band position (E_{CB}) is usually 0.1 V ~ 0.3 V lower than the Fermi level position (E_F) [53]. Therefore the position of E_{CB} is situated at -1.06 V vs. NHE for ZFO and -0.65 V vs. NHE for ZnO. Accordingly, according to the formula:

$$E_{VB} = E_{CB} + E_g \quad (3)$$

The valence band (E_{VB}) positions of ZFO and ZnO can be calculated as 0.87 V vs. NHE and 2.43 V vs. NHE, respectively.

$ZnFe_2O_4$/ZnO junction has staggered band configurations. ZFO has higher E_{CB}, E_{VB}, and E_F positions than ZnO. When ZFO and ZnO are in contact, free electrons of ZFO can transfer to ZnO until their E_F is equilibrated. The transfer of free electrons makes the ZFO side positively charged and the ZnO side negatively charged. A built-in electric field is formed on the contact surface of ZnO and ZFO, which causes the band to bend. The presence of the built-in electric field is conducive to the separation of ZnO photogenerated electrons with ZFO photogenerated holes. Photogenerated carriers with greater redox capacity are retained to participate in further reactions [54,55].

To further verify that the photogenerated carrier migration belongs to the Z-scheme charge transfer mode. We identified the active species formed during the photocatalytic reaction by the ESR technique. Under dark conditions, ZnO, ZFO, and ZZF2 can not produce •OH and $•O_2^-$ (Figure S9). After visible light irradiation ($\lambda \geq 400$ nm) for 30 s, ZZF2 samples produced •OH and $•O_2^-$ signals (Figure 8a,b). It is consistent with the results of the free radical trapping experiment and TA-PL. The signals of •OH and $•O_2^-$ were not detected by pure ZnO after 30 s of visible light irradiation (Figure 8a,b). This is due to the wide band gap of ZnO, which basically cannot absorb visible light. After ZFO irradiation, $•O_2^-$ signal was produced but no •OH signal was produced. If the photogenic holes are transferred to ZFO, ZZF2 cannot produce •OH after irradiation. This indicates that the photogenerated holes on ZnO are preserved. This is consistent with the charge transfer path of the Z-scheme heterojunction. At the same time, the $•O_2^-$ signal of the ZZF2 sample is stronger than that of ZFO, indicating that the formation of heterojunction effectively promotes the separation of photogenerated carriers.

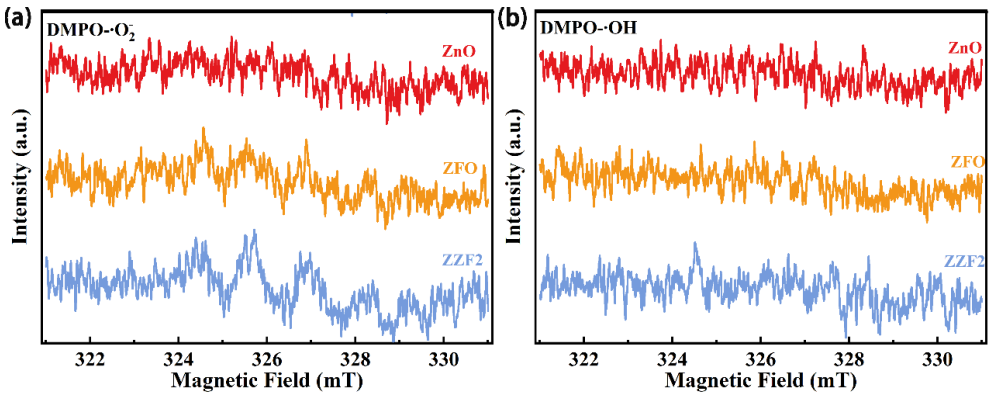

Figure 8. ESR spectra of (**a**) DMPO-•O2- and (**b**) DMPO-•OH of ZnO, ZFO and ZZF2 under visible light irradiation.

Preprints (www.preprints.org) | NOT PEER-REVIEWED | Posted: 22 September 2023 doi:10.20944/preprints202309.1580.v1

According to the above analysis, the catalytic mechanism of ZFF2 heterojunction is shown in Figure 9. The catalyst absorbs photons to form electron-hole pairs (Eq. 4). Photogenerated electrons on ZnO recombine with photogenerated holes on ZFO under the action of a built-in electric field. Photogenerated electrons on ZFO and photogenerated holes on ZnO with greater redox capacity are retained and participate in subsequent reactions (Eqs. 5-6). The nonradiative recombination of photogenerated carriers gives off heat. The introduction of thermal energy improves the separation efficiency of photogenerated carriers. Therefore, a large number of hydroxyl radicals and superoxide radicals are produced. Finally, h^+, $\bullet O_2^-$, and $\bullet OH$ oxidize the TCH (Eq. 7).

$$ZZF2 + h\nu \rightarrow h^+ + e^- \quad (4)$$

$$h^+ + \text{-}OH \rightarrow \bullet OH \quad (5)$$

$$e^- + O_2 \rightarrow \bullet O_2^- \quad (6)$$

$$h^+, \bullet OH, \bullet O_2^- + TCH \rightarrow Degraded\ \ production \quad (7)$$

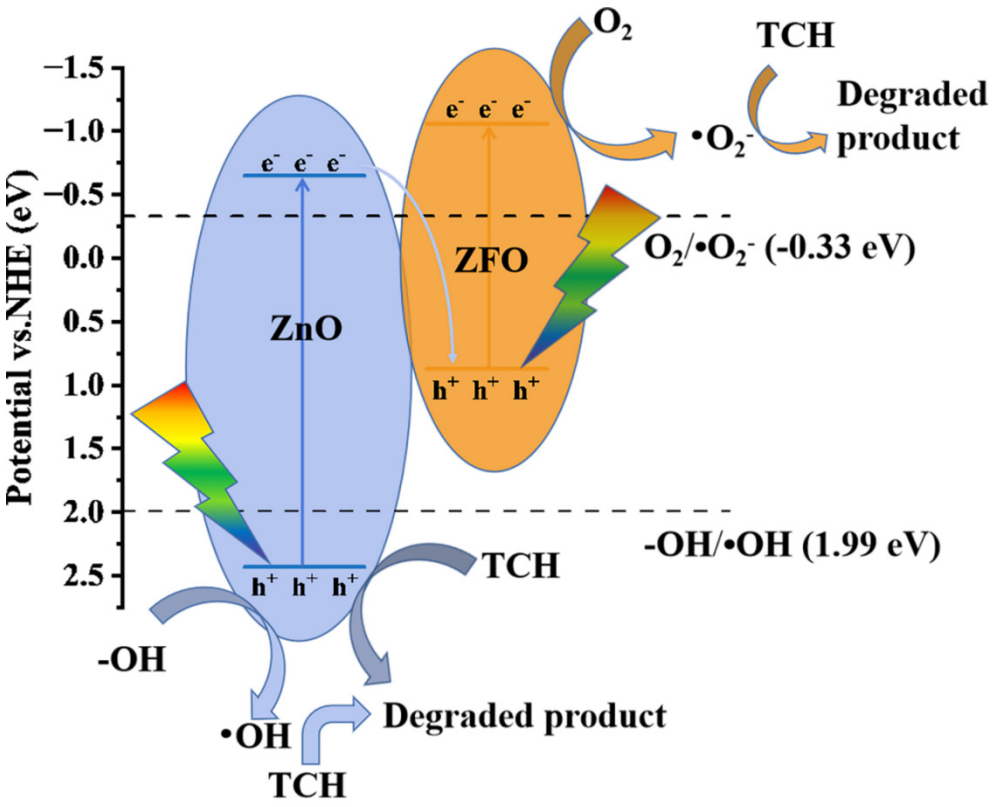

Figure 9. Mechanism of photothermal catalytic degradation of TCH over the ZZF2 heterojunction.

4. Conclusions

In summary, spindle-shaped heterojunction of Z-scheme ZnO/$ZnFe_2O_4$ is in-situ synthesized by solid phase method using MIL-88A(Fe)@Zn as the precursor. The ZZF2 sample has the highest catalytic degradation rate, with 86.3% degradation after 75 mins of visible light irradiation. It is attributed to the synergistic effect of thermo-assisted photocatalysis and thermocatalysis. Furthermore, the ZZF2 sample also has excellent catalytic activity and reusability in tap water. The Z-scheme charge transfer mechanism promotes the carrier transfer dynamics. Superoxide radicals and hydroxyl radicals are the main active species. Moreover, the catalyst can be magnetically recovered from the water. This work provides a reference for the practical application of catalysts to degrade antibiotics in wastewater.

Author Contributions: **Shilong Suo:** Conceptualization, Formal analysis, Investigation, Visualization Methodology, Writing—original draft. **Wenmei Ma:** Formal analysis, Writing—review & editing, Supervision. **Siyi Zhang:** Data curation, Formal analysis. **Ziwu Han:** Data curation, Formal analysis. **Yumin Wang:** Data curation, Formal analysis. **Yuanyuan Li:** Writing—review & editing, Supervision. **Yi Xiong:** Data curation, Formal analysis. **Yong Liu:** Data curation. **Chunqing He:** Writing—review & editing. **Pengfei Fang:** Writing—review & editing, Supervision, Funding acquisition, Project administration.

Funding: This work was financially supported by the National Key R&D Program of China (No. 2019YFA0210003) and the National Natural Science Foundation of China (No. 12275201). The authors would like to thank Prof. Jiwen Feng and Dr. Liying Wang from National Center for Magnetic Resonance in Wuhan for the ESR tests.

Institutional Review Board Statement: Not applicable.

Informed Consent Statement: Not applicable.

Data Availability Statement: Raw data is available upon request.

Conflicts of Interest: The authors declare no conflicts of interest.

Reference

1. R. Daghrir, P. Drogui, Tetracycline antibiotics in the environment: a review, *Environ. Chem. Lett.*, **2013,** *11(3),* 209-227. https://doi.org/10.1007/s10311-013-0404-8.
2. N. Barhoumi, N. Oturan, S. Ammar, A. Gadri, M.A. Oturan, E. Brillas, Enhanced degradation of the antibiotic tetracycline by heterogeneous electro-Fenton with pyrite catalysis, *Environ. Chem. Lett.*, **2017,** *15(4),* 689-693. https://doi.org/10.1007/s10311-017-0638-y.
3. I. Kim, N. Yamashita, H. Tanaka, Performance of UV and UV/H_2O_2 processes for the removal of pharmaceuticals detected in secondary effluent of a sewage treatment plant in Japan, *J. Hazard. Mater.*, **2009,** *166(2),* 1134-1140. https://doi.org/https://doi.org/10.1016/j.jhazmat.2008.12.020.
4. H.J. Liu, Y. Yang, J. Kang, M.H. Fan, J.H. Qu, Removal of tetracycline from water by Fe-Mn binary oxide, *J. Environ. Sci.*, **2012,** *24(2),* 242-247. https://doi.org/10.1016/S1001-0742(11)60763-8.
5. J.J. López-Peñalver, M. Sánchez-Polo, C.V. Gómez-Pacheco, J. Rivera-Utrilla, Photodegradation of tetracyclines in aqueous solution by using UV and UV/H_2O_2 oxidation processes, *J. Chem. Technol. Biotechnol.*, **2010,** *85(10),* 1325-1333. https://doi.org/https://doi.org/10.1002/jctb.2435.
6. D. Akhil, D. Lakshmi, P.S. Kumar, D.V.N. Vo, A. Kartik, Occurrence and removal of antibiotics from industrial wastewater, *Environ. Chem. Lett.*, **2021,** *19(2),* 1477-1507. https://doi.org/10.1007/s10311-020-01152-0.
7. D.J. Liu, B. Li, J. Wu, Y.X. Liu, Photocatalytic oxidation removal of elemental mercury from flue gas. A review, *Environ. Chem. Lett.*, **2020,** *18(2),* 417-431. https://doi.org/10.1007/s10311-019-00957-y.
8. A. Saravanan, P.S. Kumar, D.V.N. Vo, P.R. Yaashikaa, S. Karishma, S. Jeevanantham, B. Gayathri, V.D. Bharathi, Photocatalysis for removal of environmental pollutants and fuel production: a review, *Environ. Chem. Lett.*, **2021,** *19(1),* 441-463. https://doi.org/10.1007/s10311-020-01077-8.
9. X.M. Peng, W.D. Luo, J.Q. Wu, F.P. Hu, Y.Y. Hu, L. Xu, G.P. Xu, Y. Jian, H.L. Dai, Carbon quantum dots decorated heteroatom co-doped core-shell Fe-0@POCN for degradation of tetracycline via multiply synergistic mechanisms, *Chemosphere*, **2021,** *268*. https://doi.org/10.1016/j.chemosphere.2020.128806.
10. X.B. Li, J. Xiong, X.M. Gao, J. Ma, Z. Chen, B.B. Kang, J.Y. Liu, H. Li, Z.J. Feng, J.T. Huang, Novel BP/BiOBr S-scheme nano-heterojunction for enhanced visible-light photocatalytic tetracycline removal and oxygen evolution activity, *J. Hazard. Mater.*, **2020,** *387*. https://doi.org/10.1016/j.jhazmat.2019.121690.
11. B. Louangsouphom, X. Wang, J. Song, X. Wang, Low-temperature preparation of a N-TiO_2/macroporous resin photocatalyst to degrade organic pollutants, *Environ. Chem. Lett.*, **2019,** *17(2),* 1061-1066. https://doi.org/10.1007/s10311-018-00827-z.
12. J.X. Low, B.Z. Dai, T. Tong, C.J. Jiang, J.G. Yu, In Situ Irradiated X-Ray Photoelectron Spectroscopy Investigation on a Direct Z-Scheme TiO_2/CdS Composite Film Photocatalyst, *Adv. Mater.*, **2019,** *31(6)*. https://doi.org/10.1002/adma.201802981.
13. S.Y. Fang, Y.H. Hu, Thermo-photo catalysis: a whole greater than the sum of its parts, *Chem. Soc. Rev.*, **2022,** *51(9),* 3609-3647. https://doi.org/10.1039/d1cs00782c.

14. Y. Xiong, L. Huang, S. Mahmud, F. Yang, H. Liu, Bio-synthesized palladium nanoparticles using alginate for catalytic degradation of azo-dyes, *Chin. J. Chem. Eng.*, **2020,** *28(5),* 1334-1343. https://doi.org/https://doi.org/10.1016/j.cjche.2020.02.014.
15. X.M. Jia, Q.F. Han, H.N. Liu, S.Z. Li, H.P. Bi, A dual strategy to construct flowerlike S-scheme BiOBr/$BiOAc_{1-x}Br_x$ heterojunction with enhanced visible-light photocatalytic activity, *Chem. Eng. J.*, **2020,** *399*. https://doi.org/10.1016/j.cej.2020.125701.
16. X.H. He, T.H. Kai, P. Ding, Heterojunction photocatalysts for degradation of the tetracycline antibiotic: a review, *Environ. Chem. Lett.*, **2021,** *19(6),* 4563-4601. https://doi.org/10.1007/s10311-021-01295-8.
17. S. Zhang, S. Du, Y. Wang, Z. Han, X. Li, G. Li, Q. Hu, H. Xu, C. He, P. Fang, Synergy of yolk-shelled structure and tunable oxygen defect over CdS/$CdCO_3$-CoS_2: Wide band-gap semiconductors assist in efficient visible-light-driven H_2 production and CO_2 reduction, *Chem. Eng. J.*, **2023,** *454* 140113. https://doi.org/https://doi.org/10.1016/j.cej.2022.140113.
18. S. Zhang, S. Du, Y. Wang, Z. Han, W. Ma, H. Xu, Y. Lei, P. Fang, Metal-organic coordination polymers-derived ultra-small MoC nanodot/N-doped carbon combined with CdS: A hollow Z-type catalyst for stable and efficient H_2 production/CO_2 reduction, *Appl. Surf. Sci.*, **2023,** *608* 155176. https://doi.org/https://doi.org/10.1016/j.apsusc.2022.155176.
19. S. Zhang, F. Zhang, M. Yang, P. Fang, POSS modified Ni_xO_y-decorated TiO_2 nanosheets: Nanocomposites for adsorption and photocatalysis, *Appl. Surf. Sci.*, **2021,** *566* 150604. https://doi.org/https://doi.org/10.1016/j.apsusc.2021.150604.
20. S. Zhang, S. Du, Z. Han, Y. Wang, T. Jiang, S. Wu, C. Chen, Q. Han, S. Suo, H. Xu, F. Ren, P. Fang, Ohmic-functionalized type I heterojunction: Improved alkaline water splitting and photocatalytic conversion from CO_2 to C_2H_2, *Chem. Eng. J.*, **2023,** 144438. https://doi.org/https://doi.org/10.1016/j.cej.2023.144438.
21. Y. Xiong, H. Wan, M. Islam, W. Wang, L. Xie, S. Lü, S.M.F. Kabir, H. Liu, S. Mahmud, Hyaluronate macromolecules assist bioreduction (Au^{III} to Au^0) and stabilization of catalytically active gold nanoparticles for azo contaminated wastewater treatment, *Environ. Technol. Innov.*, **2021,** *24* 102053. https://doi.org/https://doi.org/10.1016/j.eti.2021.102053.
22. W. Zeng, A. Gui, X. He, M. Tang, X. Zhang, X. He, Y. Hu, K. Di, Y. Dong, Y. Xiong, P. Fang, H. Sang, Z. Chen, P. Gui, Van der Waals Black Phosphorus/$Bi_{10}O_6S_9$ Heterojunction Harvesting Ambient Electric Field Energy for Enhanced Photoelectrochemical Sense, *J. Phys. Chem. C*, **2023,** *127(2),* 1229-1243. https://doi.org/10.1021/acs.jpcc.2c07505.
23. W. Ma, M. Du, H. Li, Y. Wang, Z. Han, C. Chen, S. Zhang, Q. Han, Y. Li, J. Fang, P. Fang, The binary piezoelectric synergistic effect of $KNbO_3$/MoS_2 heterojunction for improving photocatalytic performance, *J. Alloy. Compd.*, **2023,** *960* 170669. https://doi.org/https://doi.org/10.1016/j.jallcom.2023.170669.
24. F. Guo, W. Shi, M. Li, Y. Shi, H. Wen, 2D/2D Z-scheme heterojunction of $CuInS_2$/g-C_3N_4 for enhanced visible-light-driven photocatalytic activity towards the degradation of tetracycline, *Sep. Purif. Technol.*, **2019,** *210* 608-615. https://doi.org/https://doi.org/10.1016/j.seppur.2018.08.055.
25. B. Han, Y.H. Hu, Highly Efficient Temperature-Induced Visible Light Photocatalytic Hydrogen Production from Water, *J. Phys. Chem. C*, **2015,** *119(33),* 18927-18934. https://doi.org/10.1021/acs.jpcc.5b04894.
26. Y.X. Li, M.M. Wen, Y. Wang, G. Tian, C.Y. Wang, J.C. Zhao, Plasmonic Hot Electrons from Oxygen Vacancies for Infrared Light-Driven Catalytic CO_2 Reduction on Bi_2O_{3-x}, *Angew. Chem.-Int. Edit.*, **2021,** *60(2),* 910-916. https://doi.org/10.1002/anie.202010156.
27. Z.L. Ma, W. Liu, W. Yang, W.C. Li, B. Han, Temperature effects on redox potentials and implications to semiconductor photocatalysis, *fuel*, **2021,** *286*. https://doi.org/10.1016/j.fuel.2020.119490.
28. B. Han, Y.H. Hu, Highly Efficient Temperature-Induced Visible Light Photocatalytic Hydrogen Production from Water, *J. Phys. Chem. C*, **2015,** *119(33),* 18927-18934. https://doi.org/10.1021/acs.jpcc.5b04894.
29. S. Rej, L. Mascaretti, E.Y. Santiago, O. Tomanec, Š. Kment, Z. Wang, R. Zbořil, P. Fornasiero, A.O. Govorov, A. Naldoni, Determining Plasmonic Hot Electrons and Photothermal Effects during H_2 Evolution with TiN–Pt Nanohybrids, *ACS Catal.*, **2020,** *10(9),* 5261-5271. https://doi.org/10.1021/acscatal.0c00343.
30. J.W. Li, X.Q. Yang, C.R. Ma, Y. Lei, Z.Y. Cheng, Z.B. Rui, Selectively recombining the photoinduced charges in bandgap-broken Ag_3PO_4/$GdCrO_3$ with a plasmonic Ag bridge for efficient photothermocatalytic VOCs degradation and CO_2 reduction, *Appl. Catal. B-Environ.*, **2021,** *291*. https://doi.org/10.1016/j.apcatb.2021.120053.

31. J.J. Kong, C.L. Jiang, Z.B. Rui, S.H. Liu, F.L. Xian, W.K. Ji, H.B. Ji, Photothermocatalytic synergistic oxidation: An effective way to overcome the negative water effect on supported noble metal catalysts for VOCs oxidation, *Chem. Eng. J.*, **2020,** *397*. https://doi.org/10.1016/j.cej.2020.125485.
32. F. Wang, C.H. Li, H.J. Chen, R.B. Jiang, L.D. Sun, Q. Li, J.F. Wang, J.C. Yu, C.H. Yan, Plasmonic Harvesting of Light Energy for Suzuki Coupling Reactions, *J. Am. Chem. Soc.*, **2013,** *135(15),* 5588-5601. https://doi.org/10.1021/ja310501y.
33. Z.Z. Lou, Q. Gu, Y.S. Liao, S.J. Yu, C. Xue, Promoting Pd-catalyzed Suzuki coupling reactions through near-infrared plasmon excitation of WO_{3-x} nanowires, *Appl. Catal. B-Environ.*, **2016,** *184* 258-263. https://doi.org/10.1016/j.apcatb.2015.11.037.
34. S. Sarina, H.Y. Zhu, Q. Xiao, E. Jaatinen, J.F. Jia, Y.M. Huang, Z.F. Zheng, H.S. Wu, Viable Photocatalysts under Solar-Spectrum Irradiation: Nonplasmonic Metal Nanoparticles, *Angew. Chem.-Int. Edit.*, **2014,** *53(11),* 2935-2940. https://doi.org/10.1002/anie.201308145.
35. L.C. Wang, Y. Wang, Y. Cheng, Z.F. Liu, Q.S. Guo, M.N. Ha, Z. Zhao, Hydrogen-treated mesoporous WO_3 as a reducing agent of CO_2 to fuels (CH_4 and CH_3OH) with enhanced photothermal catalytic performance, *J. Mater. Chem. A*, **2016,** *4(14),* 5314-5322. https://doi.org/10.1039/c5ta10180h.
36. X.B. Chen, L. Liu, P.Y. Yu, S.S. Mao, Increasing Solar Absorption for Photocatalysis with Black Hydrogenated Titanium Dioxide Nanocrystals, *Science*, **2011,** *331(6018),* 746-750. https://doi.org/10.1126/science.1200448.
37. B. Han, W. Wei, L. Chang, P.F. Cheng, Y.H. Hu, Efficient Visible Light Photocatalytic CO_2 Reforming of CH_4, *ACS Catal.*, **2016,** *6(2),* 494-497. https://doi.org/10.1021/acscatal.5b02653.
38. S.Y. Fang, W. Zhang, K. Sun, Y.H. Hu, Highly efficient thermo-photocatalytic degradation of tetracycline catalyzed by tungsten disulfide under visible light, *Environ. Chem. Lett.*, **2023,** *21(3),* 1287-1295. https://doi.org/10.1007/s10311-022-01526-6.
39. X.H. Zhang, B.Y. Lin, X.Y. Li, X. Wang, K.Z. Huang, Z.H. Chen, MOF-derived magnetically recoverable Z-scheme $ZnFe_2O_4/Fe_2O_3$ perforated nanotube for efficient photocatalytic ciprofloxacin removal, *Chem. Eng. J.*, **2022,** *430*. https://doi.org/10.1016/j.cej.2021.132728.
40. K. Zhang, H.Y. Cao, A. Dar, D.Q. Li, L.A. Zhou, C.Y. Wang, Construction of oxygen defective $ZnO/ZnFe_2O_4$ yolk-shell composite with photothermal effect for tetracycline degradation: Performance and mechanism insight, *Chin. Chem. Lett.*, **2023,** *34(1)*. https://doi.org/10.1016/j.cclet.2022.03.031.
41. Y.Y. Fang, Q.W. Liang, Y. Li, H.J. Luo, Surface oxygen vacancies and carbon dopant co-decorated magnetic $ZnFe_2O_4$ as photo-Fenton catalyst towards efficient degradation of tetracycline hydrochloride, *Chemosphere*, **2022,** *302*. https://doi.org/10.1016/j.chemosphere.2022.134832.
42. N. Nasseh, L. Taghavi, B. Barikbin, M.A. Nasseri, Synthesis and characterizations of a novel $FeNi_3/SiO_2/CuS$ magnetic nanocomposite for photocatalytic degradation of tetracycline in simulated wastewater, *J. Clean Prod.*, **2018,** *179* 42-54. https://doi.org/10.1016/j.jclepro.2018.01.052.
43. C. Cai, Z.Y. Zhang, J. Liu, N. Shan, H. Zhang, D.D. Dionysiou, Visible light-assisted heterogeneous Fenton with $ZnFe_2O_4$ for the degradation of Orange II in water, *Appl. Catal. B-Environ.*, **2016,** *182* 456-468. https://doi.org/10.1016/j.apcatb.2015.09.056.
44. J.Q. Li, Z.X. Liu, Z.F. Zhu, Magnetically separable ternary hybrid of $ZnFe_2O_4$-Fe_2O_3-Bi_2WO_6 hollow nanospheres with enhanced visible photocatalytic property, *Appl. Surf. Sci.*, **2014,** *320* 146-153. https://doi.org/10.1016/j.apsusc.2014.09.095.
45. W. Li, Y.J. Chen, W. Han, S.M. Liang, Y.Z. Jiao, G.H. Tian, ZIF-8 derived hierarchical $ZnO@ZnFe_2O_4$ hollow polyhedrons anchored with CdS for efficient photocatalytic CO_2 reduction, *Sep. Purif. Technol.*, **2023,** *309*. https://doi.org/10.1016/j.seppur.2022.122970.
46. H. Song, L.P. Zhu, Y.G. Li, Z.R. Lou, M. Xiao, Z.Z. Ye, Preparation of $ZnFe_2O_4$ nanostructures and highly efficient visible-light-driven hydrogen generation with the assistance of nanoheterostructures, *J. Mater. Chem. A*, **2015,** *3(16),* 8353-8360. https://doi.org/10.1039/c5ta00737b.
47. C.H. Zhang, X.Y. Han, F. Wang, L.J. Wang, J.S. Liang, A Facile Fabrication of $ZnFe_2O_4$/Sepiolite Composite with Excellent Photocatalytic Performance on the Removal of Tetracycline Hydrochloride, *Front. Chem.*, **2021,** *9*. https://doi.org/10.3389/fchem.2021.736369.
48. W.H. Fei, Y. Song, N.J. Li, D.Y. Chen, Q.F. Xu, H. Li, J.H. He, J.M. Lu, Hollow $In_2O_3@ZnFe_2O_4$ heterojunctions for highly efficient photocatalytic degradation of tetracycline under visible light, *Environ. Sci.-Nano*, **2019,** *6(10),* 3123-3132. https://doi.org/10.1039/c9en00811j.

49. B.Y. Yang, S.K. Zhang, Y. Gao, L.Q. Huang, C. Yang, Y.D. Hou, J.S. Zhang, Unique functionalities of carbon shells coating on $ZnFe_2O_4$ for enhanced photocatalytic hydroxylation of benzene to phenol, *Appl. Catal. B-Environ.*, **2022,** *304*. https://doi.org/10.1016/j.apcatb.2021.120999.
50. Z.F. Yang, X.N. Xia, L.H. Shao, L.L. Wang, Y.T. Liu, Efficient photocatalytic degradation of tetracycline under visible light by Z-scheme Ag_3PO_4/mixed-valence MIL-88A(Fe) heterojunctions: Mechanism insight, degradation pathways and DFT calculation, *Chem. Eng. J.*, **2021,** *410*. https://doi.org/10.1016/j.cej.2021.128454.
51. J. Luo, Y. Wu, X. Chen, T. He, Y. Zeng, G. Wang, Y. Wang, Y. Zhao, Z. Chen, Synergistic adsorption-photocatalytic activity using Z-scheme based magnetic $ZnFe_2O_4/CuWO_4$ heterojunction for tetracycline removal, *J. Alloy. Compd.*, **2022,** *910*. https://doi.org/10.1016/j.jallcom.2022.164954.
52. D.H. Zhu, L. Cai, Z.Y. Sun, A. Zhang, P. Heroux, H. Kim, W. Yu, Y.A. Liu, Efficient degradation of tetracycline by RGO@black titanium dioxide nanofluid via enhanced catalysis and photothermal conversion, *Sci. Total Environ.*, **2021,** *787*. https://doi.org/10.1016/j.scitotenv.2021.147536.
53. T. Cai, W.G. Zeng, Y.T. Liu, L.L. Wang, W.Y. Dong, H. Chen, X.N. Xia, A promising inorganic-organic Z-scheme photocatalyst Ag_3PO_4/PDI supermolecule with enhanced photoactivity and photostability for environmental remediation, *Appl. Catal. B-Environ.*, **2020,** *263*. https://doi.org/10.1016/j.apcatb.2019.118327.
54. L.J. Zhang, S. Li, B.K. Liu, D.J. Wang, T.F. Xie, Highly Efficient CdS/WO_3 Photocatalysts: Z-Scheme Photocatalytic Mechanism for Their Enhanced Photocatalytic H_2 Evolution under Visible Light, *ACS Catal.*, **2014,** *4(10),* 3724-3729. https://doi.org/10.1021/cs500794j.
55. Q.L. Xu, L.Y. Zhang, J.G. Yu, S. Wageh, A.A. Al-Ghamdi, M. Jaroniec, Direct Z-scheme photocatalysts: Principles, synthesis, and applications, *Mater. Today*, **2018,** *21(10),* 1042-1063. https://doi.org/10.1016/j.mattod.2018.04.008.